

ORIGINAL ARTICLE

Three-dimensional mapping of crystalline ceramic waste form materials

Alex P. Cocco¹ | Matthew B. DeGostin¹ | Jacob A. Wrubel¹ | Peter J. Damian¹ |
Tao Hong² | Yun Xu² | Yijin Liu³ | Piero Pianetta³ | Jake W. Amoroso⁴ |
Kyle S. Brinkman² | Wilson K. S. Chiu¹ 

¹Department of Mechanical Engineering,
University of Connecticut, Storrs,
Connecticut

²Department of Materials Science and
Engineering, Clemson University,
Clemson, South Carolina

³Stanford Synchrotron Radiation
Lightsource, SLAC National Accelerator
Laboratory, Menlo Park, California

⁴Savannah River National Laboratory,
Aiken, South Carolina

Correspondence

Kyle S. Brinkman, Department of
Materials Science and Engineering,
Clemson University, SC
Email: ksbrink@clemson.edu
and

Wilson K. S. Chiu, Department of
Mechanical Engineering, University of
Connecticut, Storrs, CT
Email: wchiu@engr.uconn.edu

Funding information

Nuclear Energy University Programs,
Grant/Award Number: DE-NE0008260,
CFA-14-6357; Nuclear Energy University
Program of the US Department of Energy,
Grant/Award Number: DE-NE0008260,
CFA-14-6357

Abstract

This work demonstrates the use of synchrotron-based, transmission X-ray microscopy (TXM) and scanning electron microscopy to image the 3-D morphologies and spatial distributions of Ga-doped phases within model, single- and two-phase waste form material systems. Gallium doping levels consistent with those commonly used for nuclear waste immobilization (e.g., $\text{Ba}_{1.04}\text{Cs}_{0.24}\text{Ga}_{2.32}\text{Ti}_{5.68}\text{O}_{16}$) could be readily imaged. The analysis suggests that a minority phase with different stoichiometry/composition from the primary hollandite phase can be formed by the solid-state ceramic processing route with varying morphology (globular vs. cylindrical) as a function of Cs content. The results presented in this work represent a crucial step in developing the tools necessary to gain an improved understanding of the microstructural and chemical properties of waste form materials that influence their resistance to aqueous corrosion. This understanding will aid in the future design of higher durability waste form materials.

KEYWORDS

nuclear waste, processing, scanning electron microscopy, synchrotron, transmission X-ray microscopy, X-ray computed tomography

1 | BACKGROUND

Durable ceramic waste forms that incorporate a wide range of radionuclides have the potential to broaden the available disposal options and to lower the storage and disposal costs associated with advanced fuel cycles.¹ These materials, originally developed by Ringwood et al.,² are often referred to as SYNROC (short for “Synthetic Rock”). SYNROC materials comprise ceramic waste forms that are tailored to mimic certain minerals (i.e., unique crystalline

structures) that are known to host radionuclides by binding them into specific crystalline networks.^{2,3} Ceramic waste form material design is guided by knowledge of naturally occurring minerals, which contain similar radioactive and nonradioactive species as found in waste generated from commercial used nuclear fuel (UNF) reprocessing and weapons production.^{4,5}

In an aqueous reprocessing scenario, four primary waste streams are typically considered: (i) a Cs/Sr separated stream, (ii) a waste stream consisting of *lanthanide fission products*,

(iii) a *transition metal fission product* waste stream resulting from transuranic extraction, and (iv) residual, unrecovered *minor actinides*.⁶ Many elements in the aqueous reprocessing waste stream are known to react with select additives to form stable SYNROC (titanate-based) crystalline phases of the types hollandite,⁷ perovskite/pyrochlore,⁸ and zirconolite.^{9,10} Such materials are typically densified via hot isostatic pressing (HIP). Recent work, however, has shown that they can also be produced from a melt.¹¹⁻¹³

A greater understanding of the influence of processing conditions on the elemental partitioning, microstructural features, and connectivity of the phases of ceramic waste forms is needed to better design and exploit their properties. Moreover, an understanding of the link between 3-D features of a waste form material's microstructure and its corrosion behavior is needed to assess its long-term performance. For instance, residual porosity connected to the material's surface increases the surface area available for corrosion. Similarly, in multiphase systems, the preferential corrosion of a particular phase can lead to increased porosity and, in turn, increased corrosion-vulnerable surface area. In both cases, the 3-D spatial distribution of phases (including pores) as well as their 3-D morphologies significantly influence the waste form's corrosion behavior. Therefore, to better understand the influence of microstructure on corrosion behavior, imaging techniques are required that, at a minimum, have the capability to (i) discern multiple phases and to (ii) reveal each phase's spatial distribution, morphology, and connectivity in 3-D.

A number of 3-D imaging techniques exist and in recent years they have seen increasingly rapid development and widespread application in the study of "energy materials" (i.e., materials used in energy conversion and storage technologies).¹⁴ Similar to SYNROC, energy material design benefits from an understanding of how 3-D microstructural features influence performance. In choosing a 3-D imaging technique to study ceramic waste form materials, two additional criteria are required. The technique must be (i) capable of imaging dense (i.e., high Z) materials and it must (ii) offer 3-D resolution on the order of ten's of nanometers with a field of view large enough to image volumes on the order of hundreds of cubic micrometers.

This work demonstrates synchrotron-based, X-ray nanotomography (XNT) as a viable technique for discerning and imaging in 3-D multiple phases in waste form material systems. The technique's nondestructive image acquisition, which permits the ready application of complimentary characterization techniques, and its potential for in situ imaging in future experiments were significant in choosing XNT. Further discussion regarding the choice of XNT for this study can be found in the online Supplementary Material.

In this work, the use of XNT in conjunction with complimentary electron- and X-ray-based techniques (i.e., XRD and

SEM-EDS) is shown to offer a powerful means of obtaining insight into 3-D phase morphology and spatial variations in composition. Specifically, SEM-EDS and synchrotron-based absorption contrast XNT revealed compositional variations in single-phase, Ga-doped, Cs-containing hollandite.

2 | INTRODUCTION: MATERIALS

A Cs-containing hollandite system was synthesized for 3-D, X-ray-based imaging. Hollandite-type compounds, generally expressed as $A_xM_8O_{16}$, are widely proposed to host and to immobilize Cs in a crystalline waste form.¹⁵⁻¹⁷ Based on current Department of Energy Office of Nuclear Energy waste streams from potential commercial fuel recycling scenarios, hollandite comprises a large volume fraction of the phase assemblage in multiphase waste forms, and its phase formation is deemed critical to the overall integrity of the waste form material.⁶

Model waste form material systems consisting of (i) Ga-doped, single-phase hollandite and (ii) two-phase hollandite+TiO₂ were synthesized using solid-state ceramic processing of oxide powders. In addition to favorable X-ray absorption characteristics, Ga⁺³ is stable in reducing and oxidizing atmospheres and it decreases the hollandite's melting temperature.

Three Ga-containing, single-phase hollandite compounds were synthesized: (i) Ba_{1.33}Ga_{2.66}Ti_{5.34}O₁₆ (no Cs), (ii) Ba_{1.04}Cs_{0.24}Ga_{2.32}Ti_{5.68}O₁₆ (intermediate Cs content), and (iii) Ba_{0.667}Cs_{0.667}Ga₂Ti₆O₁₆ (highest Cs content). These compositions were intended to provide insight into the phase formation and microstructural evolution of pure Ba hollandite and of hollandite with varying amounts of Cs.

Owing to its simplicity and prevalence in realistic multiphase waste forms, titanium oxide (TiO₂) was selected as the second component for the model two-phase systems. The hollandite-TiO₂ materials were fabricated in both dense and porous forms to evaluate the ability of the imaging technique to discriminate residual porosity. The images collected in this study demonstrate that Ga is an effective dopant for synchrotron-based X-ray imaging of these materials. The specific imaging technique used in this work was synchrotron-based differential X-ray absorption contrast nanotomography.

3 | DIFFERENTIAL X-RAY ABSORPTION CONTRAST NANOTOMOGRAPHY

Synchrotron-based differential X-ray absorption contrast nanotomography makes use of a transmission X-ray microscope, which is shown schematically in Figure 1A. Upstream

from the microscope, a synchrotron X-ray source and monochromator (not pictured) provide the TXM with a monochromatic beam of X-rays, which is directed by a capillary condenser through a pinhole and onto the sample, which sits on a rotation stage and is fully illuminated by the beam (as opposed to a configuration in which a small-diameter beam scans across the sample). The X-rays transmitted through the sample are focused onto a CCD X-ray detector by a Fresnel zone plate. A three-dimensional image of a sample is obtained by rotating it and collecting images at small angular increments. The series of 2-D images, called “projection images,” are then “tomographically reconstructed” to yield a 3-D image of the sample.^{18,19}

Contrast in TXM images reflects variations in the linear X-ray absorption (or “x-ray attenuation”) coefficients of the

elements within the sample. The absorption coefficient is a material property, which in Beer’s Law determines the proportion of an incident X-ray’s energy that is absorbed as it passes through a given length of material. Thus, darker regions in a TXM image correspond to locations within the sample that contain elements with greater attenuation coefficients. In this work, the images are presented in so-called “reverse contrast mode,” whereby the opposite of the previous statement is true, that is, darker regions indicate the presence of elements with *smaller* attenuation coefficients.

Differential contrast imaging relies on identifying features of an element’s X-ray absorption spectrum called “absorption edges.” Absorption edges occur at X-ray energies where the element’s absorption behavior exhibits a discontinuity. Consider, for example, Figure 1B, which shows

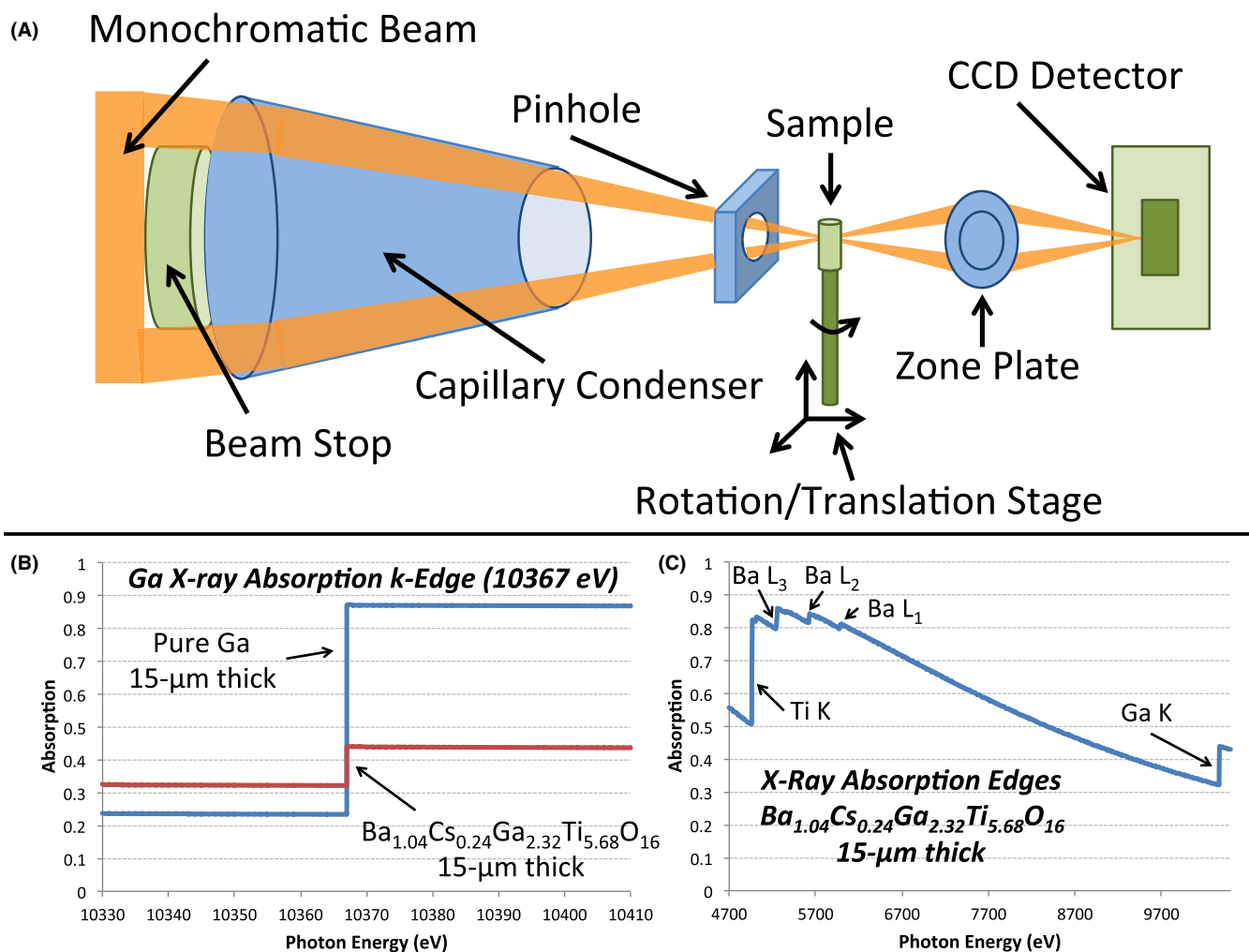


FIGURE 1 A, Schematic of a transmission X-ray microscope (TXM). B, Calculated X-ray absorption for 15- μm -thick samples of pure Ga (blue) and a common Cs-containing hollandite ($\text{Ba}_{1.04}\text{Cs}_{0.24}\text{Ga}_{2.32}\text{Ti}_{5.68}\text{O}_{16}$) (red). Ga’s X-ray absorption k-edge is at ~ 10.367 keV. Because the magnitude of the absorption change across the edge depends on Ga content, the change for the hollandite phase is less than that for pure Ga. C, Calculated X-ray absorption through a 15- μm -thick section of hollandite ($\text{Ba}_{1.04}\text{Cs}_{0.24}\text{Ga}_{2.32}\text{Ti}_{5.68}\text{O}_{16}$). The elemental absorption edges for its constituent elements are indicated. Ga’s k-edge offers the best combination of (1) a relatively large change in absorption and (2) a sufficient photon flux. Calculation of the absorption curves was performed using the CXRO calculator (http://henke.lbl.gov/optical_constants)

Ga's X-ray absorption k-edge at 10 367 eV and which was obtained using the CXRO calculator for X-ray Interactions with Matter (http://henke.lbl.gov/optical_constants). Gallium is significantly more attenuating for incident X-ray beams whose energies are greater than 10 367 eV. Importantly, this jump in absorption behavior is *characteristic* of Ga (specifically of Ga's k electron shell). Therefore, if a Ga-containing sample is imaged just above and just below the Ga k-edge, then regions within the sample containing Ga will exhibit significantly different contrast in the collected images. This element identification procedure is known as "differential x-ray absorption contrast imaging."

The technique can be performed using the absorption edge(s) of any element within a given sample. Figure 1C, for example, shows X-ray absorption edges for elements contained with the model waste form materials studied in this work. We chose to image across the Ga edge because (i) it exhibits a significant change in absorption and (ii) it is located at a photon energy for which the TXM was able to provide a sufficient photon flux. Imaging at the Ti edge, for instance, would have involved reducing the incident X-ray energy to a level that limits the photon flux, which in turn would have made it necessary to dramatically increase the exposure time per image and/or to contain the sample in helium as a way to minimize X-ray attenuation in air.

An important aspect of absorption contrast imaging is that the magnitude of the contrast change observed in images collected above and below an elemental absorption edge depends on the concentration of that element. Compare, for instance, in Figure 1A the change in transmission predicted for pure Ga to that predicted for a 15-micrometer-thick sample of the Cs-containing, Ga-doped hollandite material ($\text{Ba}_{1.04}\text{Cs}_{0.24}\text{Ga}_{2.32}\text{Ti}_{5.68}\text{O}_{16}$). The change in transmission for pure Ga is nearly 65%, whereas the change expected for the

hollandite material is closer to 10%; the higher the concentration of Ga, the greater the contrast change.

By combining absorption contrast imaging with tomography it is possible to map the spatial distribution and relative concentrations of various elements within a sample in 3-D. In this work, Ga is mapped within ceramic waste form material systems. For more in-depth discussion of differential X-ray absorption contrast nanotomography including considerations for sample preparation, please see the online Supplemental Material.

4 | EXPERIMENT

4.1 | Sample preparation

Three hollandite compositions were considered: (i) $\text{Ba}_{1.33}\text{Ga}_{2.66}\text{Ti}_{5.34}\text{O}_{16}$ (no Cs); (ii) $(\text{Ba}_{0.667}\text{Cs}_{0.667}\text{Ga}_2\text{Ti}_6\text{O}_{16})$ (highest Cs content); and (iii) $\text{Ba}_{1.04}\text{Cs}_{0.24}\text{Ga}_{2.32}\text{Ti}_{5.68}\text{O}_{16}$ (intermediate Cs content typically found in the literature).¹⁷ The hollandite was synthesized by solid-phase reaction. BaCO_3 , Cs_2CO_3 , Ga_2O_3 , and TiO_2 (all from Sigma-Aldrich, St. Louis, MO, USA; >99.9%) were mixed in stoichiometry and then ball-milled in ethanol with ZrO_2 milling media for 24 h. The powders were dried and calcined at 1200°C for 10 h to form the hollandite phase.

Hollandite pellets were prepared by uniaxially pressing hollandite powders and then sintering them at 1300°C for 2 h to densify the resulting composite. (Due to the sintering activity of $\text{Ba}_{0.667}\text{Cs}_{0.667}\text{Ga}_2\text{Ti}_6\text{O}_{16}$ and $\text{Ba}_{1.04}\text{Cs}_{0.24}\text{Ga}_{2.32}\text{Ti}_{5.68}\text{O}_{16}$, it was not possible to prepare a completely dense sample.) For the dense, two-phase hollandite– TiO_2 system, 20 wt% TiO_2 was added to the hollandite powder, the mixture was ball milled, and then sintered at 1300°C for 2 h. For the porous, two-phase hollandite– TiO_2 sample, 10 wt% graphite was added as a pore former (Table 1).

4.2 | Characterization of phase composition and microstructure

The samples' phase structures were characterized by X-ray diffraction (Rigaku TTR-III; Rigaku, Woodlands, TX, USA)

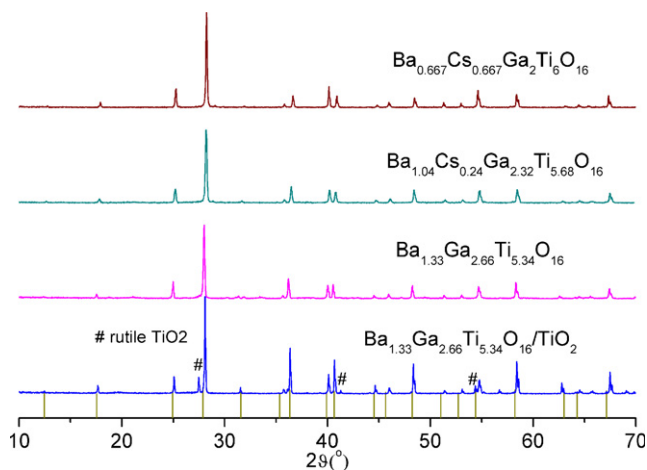


FIGURE 2 XRD patterns for dense hollandite samples synthesized by sintering at 1300°C for 2 h

TABLE 1 Density and volume fractions for single-phase hollandite and two-phase hollandite– TiO_2 samples

Composition	Density	Hollandite/ TiO_2 Volume Fractions
$\text{Ba}_{1.33}\text{Ga}_{2.66}\text{Ti}_{5.34}\text{O}_{16}$	Dense	1.0/0.0
$\text{Ba}_{0.667}\text{Cs}_{0.667}\text{Ga}_2\text{Ti}_6\text{O}_{16}$	Porous	1.0/0.0
$\text{Ba}_{1.04}\text{Cs}_{0.24}\text{Ga}_{2.32}\text{Ti}_{5.68}\text{O}_{16}$	Porous	1.0/0.0
$\text{Ba}_{1.33}\text{Ga}_{2.66}\text{Ti}_{5.34}\text{O}_{16}/\text{TiO}_2$	Dense	0.8/0.2
$\text{Ba}_{1.33}\text{Ga}_{2.66}\text{Ti}_{5.34}\text{O}_{16}/\text{TiO}_2$	Porous	0.8/0.2

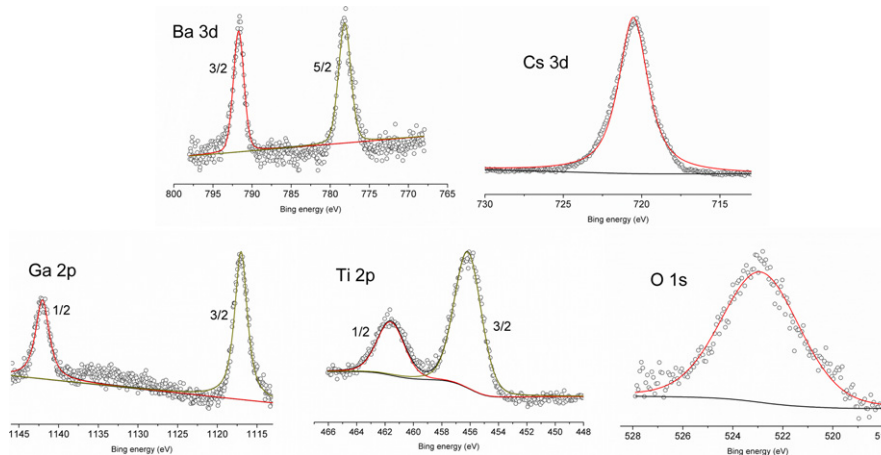


FIGURE 3 XPS spectra (Ba 3d, Cs 3d, Ga 2p, Ti 2p, and O 1s) of the $\text{Ba}_{0.667}\text{Cs}_{0.667}\text{Ga}_2\text{Ti}_6\text{O}_{16}$ (highest Cs content) pellet surface. (Black circles=measured data; black line=the sum of fits; red/yellow dotted lines=components)

The first column of Figure 4 shows a representative, reconstructed cross section of a $\text{Ba}_{1.33}\text{Ga}_{2.66}\text{Ti}_{5.34}\text{O}_{16}$ sample imaged above and below the Ga k-edge. Because both cylindrical samples yielded virtually identical results with respect to the homogeneity of Ga doping and to the contrast change observed across the Ga k-edge, results for only one sample are presented. The hollandite's Ga doping is largely homogeneous with some regions of higher Ga content (approximately 2% of the sample volume) indicated by starker contrast change across the edge. The regions of higher Ga content were found most often around pores (which accounted for ~1% of the volume). Segmentation of the sample, as shown in Figure 4, revealed that the Ga-rich regions exhibit globular morphology, which can be seen in Figure 5A, the full 3-D rendering of the sample, and for an isolated example region in the bottom portion of Figure 5D. Additional cross sections from this sample can be viewed in the online Supplementary Materials.

As stated above, because the baseline sample does not contain Cs, the Ga inhomogeneity cannot be attributed to the Cs-induced formation of secondary phases. Another possible explanation is that the variations were introduced during sample preparation by the Ga FIB. To rule out this possibility, an additional sample of the same composition was prepared using a plasma FIB with a Xe-ion beam (FEI Helios P-FIB; FEI, Hillsboro, OR, USA) and then imaged during a later experiment. The resulting images (shown in the online Supplementary Materials) also exhibited regions of higher Ga intensity, again close to pores and with globular morphology, thus ruling out Ga implantation during FIB milling as their cause.

A more likely explanation for the Ga-rich regions is that they resulted from relatively aggressive Ga doping. To obtain maximum contrast change across the Ga absorption edge, high Ga-content hollandite stoichiometries were

targeted. The baseline composition $\text{Ba}_{1.33}\text{Ga}_{2.66}\text{Ti}_{5.34}\text{O}_{16}$ contained close to the maximum Ga concentration expected to be stable in the crystal system, and therefore the material may have not fully developed into a homogeneously pure phase,²³ which resulted in the formation of globular regions of higher Ga content especially around pores.

The vast majority of the imaged material, however, appears to have been uniformly doped (again Ga-rich regions accounted for ~2% of the imaged volume) and the pixel intensity for the majority of the hollandite phase changed by roughly 10% across the k-edge. Thus, despite isolated regions of nonuniform Ga doping, the images of the $\text{Ba}_{1.33}\text{Ga}_{2.66}\text{Ti}_{5.34}\text{O}_{16}$ sample suggest that Ga doping does in fact provide an effective means of marking hollandite phases for the absorption contrast-based X-ray imaging of waste form materials.

5.2 | TXM results for Cs-containing samples: ($\text{Ba}_{1.04}\text{Cs}_{0.24}\text{Ga}_{2.32}\text{Ti}_{5.68}\text{O}_{16}$) & ($\text{Ba}_{0.667}\text{Cs}_{0.667}\text{Ga}_2\text{Ti}_6\text{O}_{16}$)

Two hollandite samples with differing Cs content were imaged: (i) a composition typically found in the literature ($\text{Ba}_{1.04}\text{Cs}_{0.24}\text{Ga}_{2.32}\text{Ti}_{5.68}\text{O}_{16}$), and (ii) a composition of higher Cs content ($\text{Ba}_{0.667}\text{Cs}_{0.667}\text{Ga}_2\text{Ti}_6\text{O}_{16}$). Like the images of the baseline samples, images of the Cs-containing samples, shown in the second and third columns of Figure 4, reveal a nonuniform distribution of Ga. There is, however, in addition to the globular Ga-rich regions, another type of Ga variation: namely, rod-like regions of Ga content higher than the majority of the material volume (~35% contrast change vs. a ~10% contrast change across the edge) but less than that of the globular regions (which exhibited a contrast change of ~48% across the edge). In the segmented cross sections shown in Figure 4, the rods appear as elliptical

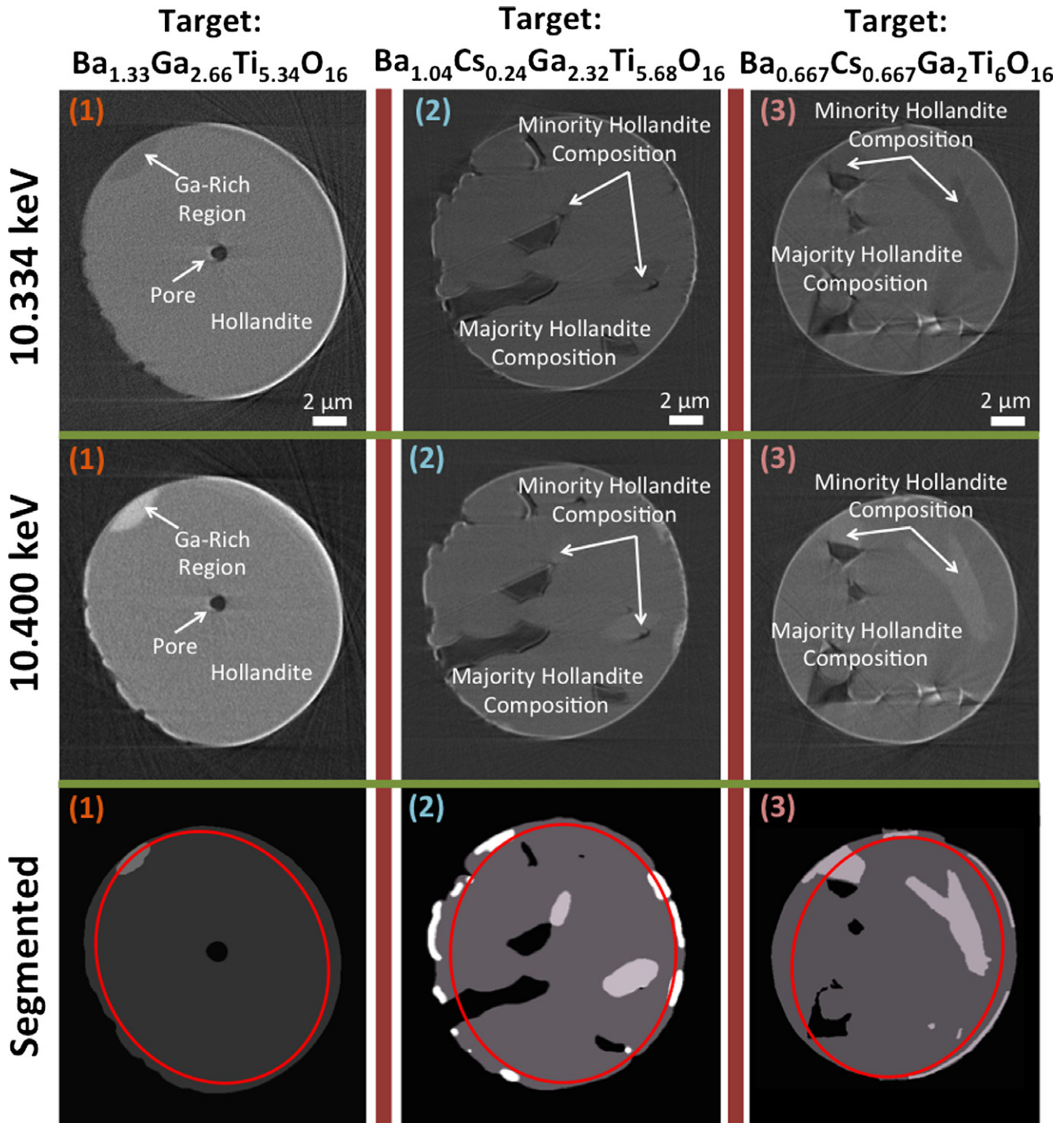


FIGURE 4 Below-edge (10.334 keV), above-edge (10.400 keV), and segmented images of representative cross sections of (1) the baseline hollandite without Cs; (2) the intermediate Cs composition hollandite; and (3) the highest Cs composition hollandite. The red ellipses in the segmented images indicate where the volumes were cropped to generate the renderings in Figure 5.

regions. In the highest Cs-content sample, the region resembling a “y” corresponds to two intersection rods, which intersect the given cross section at different angles.

Both types of regions were in the intermediate Cs-content sample and can be seen in the 3-D renderings shown in Figure 5B where the Ga-rich, globular regions (~2% of

the volume) are shown in green and the rod-like “minority hollandite” (~1% of the volume) in red. The “majority hollandite” is shown in blue and has been rendered transparent such that the porosity, the green, and the red phases are viewable. The porosity accounted for ~11% of the imaged volume of the intermediate Cs-content sample.

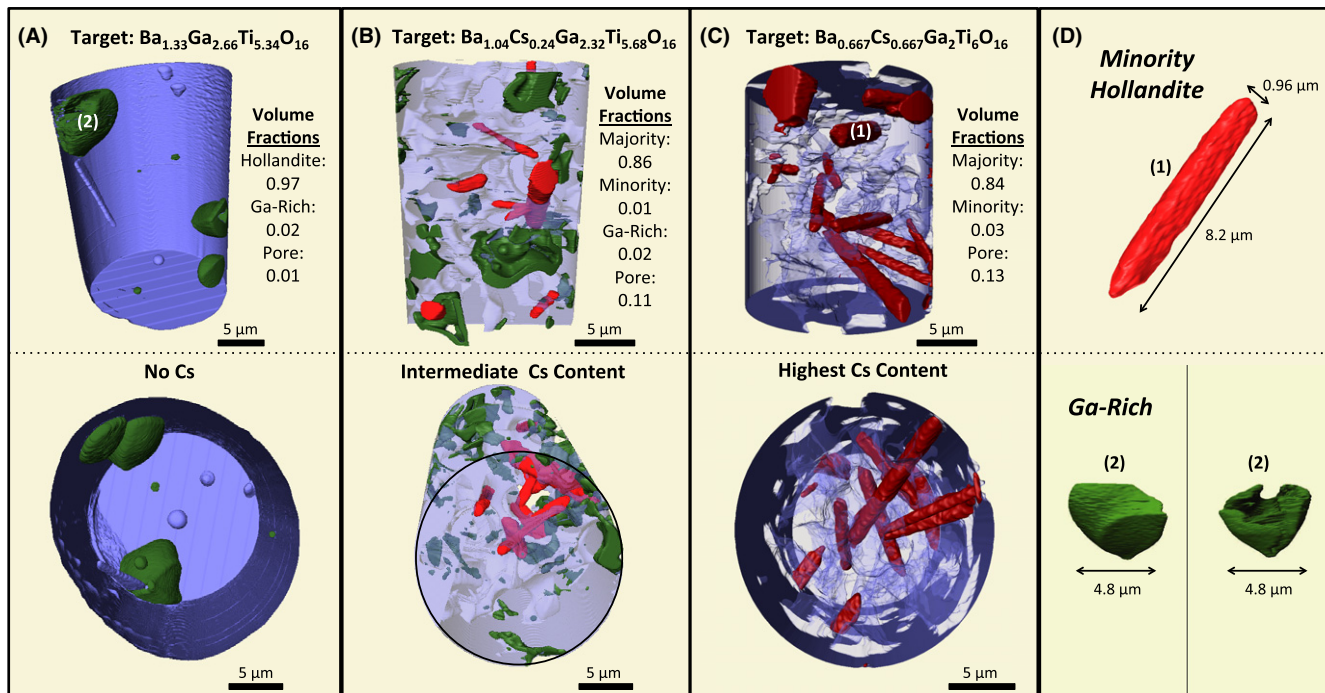


FIGURE 5 3-D visualization of the single-phase hollandite (A) without Cs ($\text{Ba}_{1.33}\text{Ga}_{2.66}\text{Ti}_{5.34}\text{O}_{16}$), (B) with intermediate Cs content ($\text{Ba}_{1.04}\text{Cs}_{0.24}\text{Ga}_{2.32}\text{Ti}_{5.68}\text{O}_{16}$), and (C) with higher Cs content ($\text{Ba}_{0.667}\text{Cs}_{0.667}\text{Ga}_2\text{Ti}_6\text{O}_{16}$). Panel (D) shows the two types of differing Ga-content regions found in the samples. The rod-like region in the upper panel was isolated from the higher Cs-content sample and the globular region was taken from the baseline sample without Cs. The intermediate Cs sample is the only one of the three that contains both types of regions

In the higher Cs sample, shown in Figure 4 and rendered in Figure 5C, all Ga-rich regions were rod-like and accounted for approximately 3% of the sample volume (with porosity about 13%). The largest complete rod of the minority hollandite in the highest Cs-content sample has been isolated and rendered in the upper portion of Figure 5D to clearly illustrate the morphological difference between the minority hollandite and the globular, Ga-rich regions.

Further analysis of the rod-like Ga-rich regions is provided after discussion of the two-phase waste form systems. In the additional analysis, a combination of electron-based microscopy, spectroscopy, and additional analysis of the X-ray images suggests that the “majority” and “minority hollandite” phases are a local variation in the composition of the single-phase hollandite. The rod-like microstructure of the minority hollandite, which was found to be Cs and Ga rich, is consistent with literature reports of enhanced growth along the [100] tunnel direction in hollandite with increasing Cs.^{17,24} Before proceeding to further analysis of the single-phase hollandite, however, the remainder of this section presents the X-ray imaging results for the two-phase model waste form systems, which were intended to demonstrate the ability of the technique to discern two solid phases from pore in waste form material systems.

5.3 | Two-phase model systems: dense and porous hollandite/ TiO_2 materials

This set of results show images of two-phase, hollandite/ TiO_2 waste form systems. Two dual-phase materials were synthesized: (i) a dense and (ii) a porous hollandite/ TiO_2 material, each with the composition $\text{Ba}_{1.33}\text{Ga}_{2.66}\text{Ti}_{5.34}\text{O}_{16}/\text{TiO}_2$. In these images, the primary hollandite and TiO_2 phases are discernable from one another, and, in addition, there appear to be multiple regions of varying Ga content, which are clearly seen in the reconstructed cross sections. The hollandite in these samples does not contain Cs. Therefore, the Ga-rich regions observed in these samples do not exhibit the rod-like morphology observed in the Cs-containing hollandite examined in the previous section.

5.4 | Dense hollandite/ TiO_2

Figure 6 shows a reconstructed cross-section obtained at each energy level for the dense $\text{Ba}_{1.33}\text{Ga}_{2.66}\text{Ti}_{5.34}\text{O}_{16}/\text{TiO}_2$ material. The hollandite phase is clearly discernable from the TiO_2 . A slight contrast change exhibited by the TiO_2 indicates that Ga incorporated into both phases. Aliovalent Ga doping, Ga^{+3} on Ti^{+4} sites is well known in these materials and low Ga levels in TiO_2 were expected to result from the diffusion of Ga during high-temperature

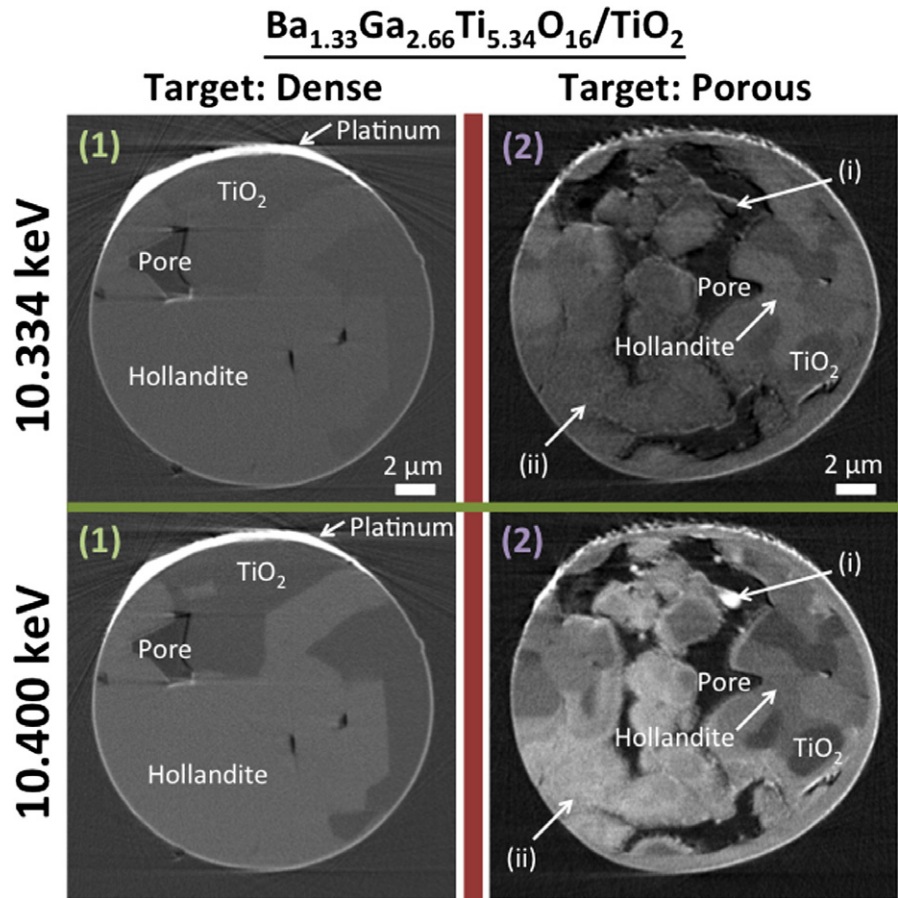


FIGURE 6 Below-edge (10.334 keV) and above-edge (10.400 keV) images of representative cross sections of (1) the dense and (2) the porous hollandite+TiO₂ model waste form material systems

sintering.²⁵ The very bright region labeled “Platinum” is a thin layer of Pt, the material used to secure the samples onto the tips of pins, which were mounted into the TXM.

5.5 | Porous hollandite/TiO₂

Figure 6 presents a representative cross section obtained from 1 of 2 samples that were imaged of the porous, two-phase hollandite $\text{Ba}_{1.33}\text{Ga}_{2.66}\text{Ti}_{5.34}\text{O}_{16}/\text{TiO}_2$ waste form material. The porous, two-phase system contained many more regions of varying Ga content than the previous samples. In the $\text{Ba}_{1.33}\text{Ga}_{2.66}\text{Ti}_{5.34}\text{O}_{16}$ hollandite samples, globular Ga-rich regions were observed to occur most often around pores. Increasing the porosity of the system and introducing a second phase (the TiO₂) acts to increase the interfacial area of the hollandite per volume. This could have made the material more susceptible to Ga inhomogeneity.

The images of the two-phase model systems demonstrate the ability of the X-ray imaging technique to discern many regions of varying Ga concentration. To fully understand the imaging results, however, additional complementary analysis is required. In the following section, further analysis of the rod-like Ga-rich phase observed in the Cs-containing single-phase hollandite samples is performed,

which reveals additional insight into the composition of the phase.

5.6 | Imaging artifacts, segmentation, and volume fraction Estimates

Before moving on, it is important to comment on imaging artifacts in the TXM images presented above. The artifacts are as follows: (i) a thin higher contrast layer around the perimeter of the sample in the reconstructed cross sections, and (ii) slight “haloing” and “streaking” effects that occurs near the pore/solid interfaces. As mentioned above, it was confirmed by milling additional samples using a Xe plasma FIB that Ga implantation is not responsible for the Ga-rich regions observed within the samples’ volumes. It is, however, likely the source of the high contrast ring around the samples’ perimeters. These thin rings exhibit a contrast change across the Ga k-edge and, therefore, must contain Ga. Rings around the border of the sample are removed during segmentation by simply cropping the volume as indicated in Figure 4 by the red ellipses.

The haloing artifacts that occur around pore–solid interfaces likely result from refraction of the X-rays and are more difficult to remove by segmentation. In this work, haloing was minimized by performing successive erosions

and dilations of the segmented image. An erosion involves reducing the size of a given feature by uniformly subtracting a layer of predefined voxel thickness. Dilation is the exact opposite procedure. Erosion can remove thin regions in the segmented image that result from halting artifacts. Once these regions are eroded away, the image is then dilated back to its original proportion. The erosion/dilation procedure comes at the cost of rounding sharp points or edges within the image, which is evident in the sample cross sections in Figure 4. In addition, the sizes of various features within the material may be exaggerated; for example, the pore in the first column of Figure 4 is slightly larger in the segmented image compared to the “raw” cross section.

The streak artifacts are the result of X-ray diffraction, which resulted as incident X-rays satisfied the Bragg condition for certain grains within the material. Bragg diffraction was clearly observed in the projection images; bright areas in the image suddenly appeared for particular sample orientations and disappeared as soon as the angle of the sample relative to the beam changed. There was negligible change in contrast across the Ga *k*-edge for the streak regions, indicating that they are indeed artifacts and not caused by local Ga concentration variation. The streak artifacts were readily addressed by image segmentation techniques; specifically, by applying filters to the image.

Given the image artifacts and segmentation procedures given above, the question arises: How reliable are the volume fraction values estimated from these images? The answer to this question involves three primary sources of error: (i) the resolution of the TXM; (ii) the representativeness of the sample; and (iii) the segmentation procedure. Let us consider each in order.

Given that (i) the overwhelming majority of Ga-rich and rod-like regions have dimensions on the order of 10's of voxels and that (ii) both exhibited very distinct contrast in the projection images, it is not unreasonable to assume that the first potential source of error, the TXM's resolution, is negligible.

The second source of possible error relating to the representativeness of the sample cannot be quantified from the current study because only a single sample was imaged for each Cs content. Therefore, it is not possible to measure how representative the phase spatial distribution and volume fraction in each imaged cylinder is of the larger sample of material. The complementary EDS measurements, however, confirm that the minority hollandite composition must be ubiquitous within the material.

The last potential source of error, the segmentation procedure, can be approximately assessed by dilating and eroding each phase by a predefined voxel thickness. This method provides an approximate sense of how an over- and underrepresentation of a given phase would change its

volume fraction. Applying this procedure to the minority hollandite composition in each Cs-containing sample, it was found that, given a voxel thickness of 2 voxels, the minority composition's volume fraction could change by approximately ± 0.01 , which is on the same order of magnitude as the volume fraction estimates themselves.

Taking these considerations together, it can be concluded that the relative magnitudes of the volume fractions of the phases within a given sample are likely reliable. Trends that rely on comparing across samples, however, cannot be identified with high confidence. Specifically, the apparent trend that as Cs content increases, the volume fraction of Ga-rich regions decreases and that of the minority hollandite composition increases is only suggested by this data. Further investigation is required to confirm it.

6 | MAJORITY AND MINORITY HOLLANDITE PHASES

As pointed out in the TXM result, the rod-like Ga-rich phase occupied ~2% and 3% in the intermediate and high Cs-content hollandite samples, respectively. The XRD results presented earlier, however, did not reveal any secondary phases within the detection limit of the technique. This is likely because the detection sensitivity of the XRD technique is approximately 5% volume fraction. SEM-EDS analysis of these samples also did not reveal significant elemental partitioning or segregation to indicate secondary-phase formation. Together, these results suggest that the Ga-rich phase observed in the TXM images is a single hollandite phase with regions of varying Ga content.

To confirm the composition of the Ga-rich phase, SEM-EDS was employed to analyze $\text{Ba}_{0.667}\text{Cs}_{0.667}\text{Ga}_2\text{Ti}_6\text{O}_{16}$ and $\text{Ba}_{1.04}\text{Cs}_{0.24}\text{Ga}_{2.32}\text{Ti}_{5.68}\text{O}_{16}$ pellets, as shown in Figure 7. In the mapping result, Ba, Cs, Ti, and O were distributed uniformly on the surface. However, Ga exhibited bright spots in the elemental maps. These brighter signals indicate a higher elemental ratio, which is consistent with the TXM result. Estimates of the compositions of the Ga-rich areas were obtained from 10 different points within the microstructure by EDS as shown in Figure 8. The EDS point results were recalculated normalizing to Ti (i.e., the Ti stoichiometry was set as the target value). The calculated results from averaging the values over the 10 points are displayed in Table 2.

Results for the $\text{Ba}_{0.667}\text{Cs}_{0.667}\text{Ga}_2\text{Ti}_6\text{O}_{16}$ sample (the higher Cs content) indicate that the stoichiometry of Ba, Cs, and Ga in the majority phase was 0.633, 0.592, and 1.93, respectively, which is close to the target values 0.667, 0.667, and 2. The $\text{Ba}_{1.04}\text{Cs}_{0.24}\text{Ga}_{2.32}\text{Ti}_{5.68}\text{O}_{16}$ sample (the intermediate Cs content) displayed similar results for the majority phase. In the minority phase, however, the ratios of Ba, Cs,

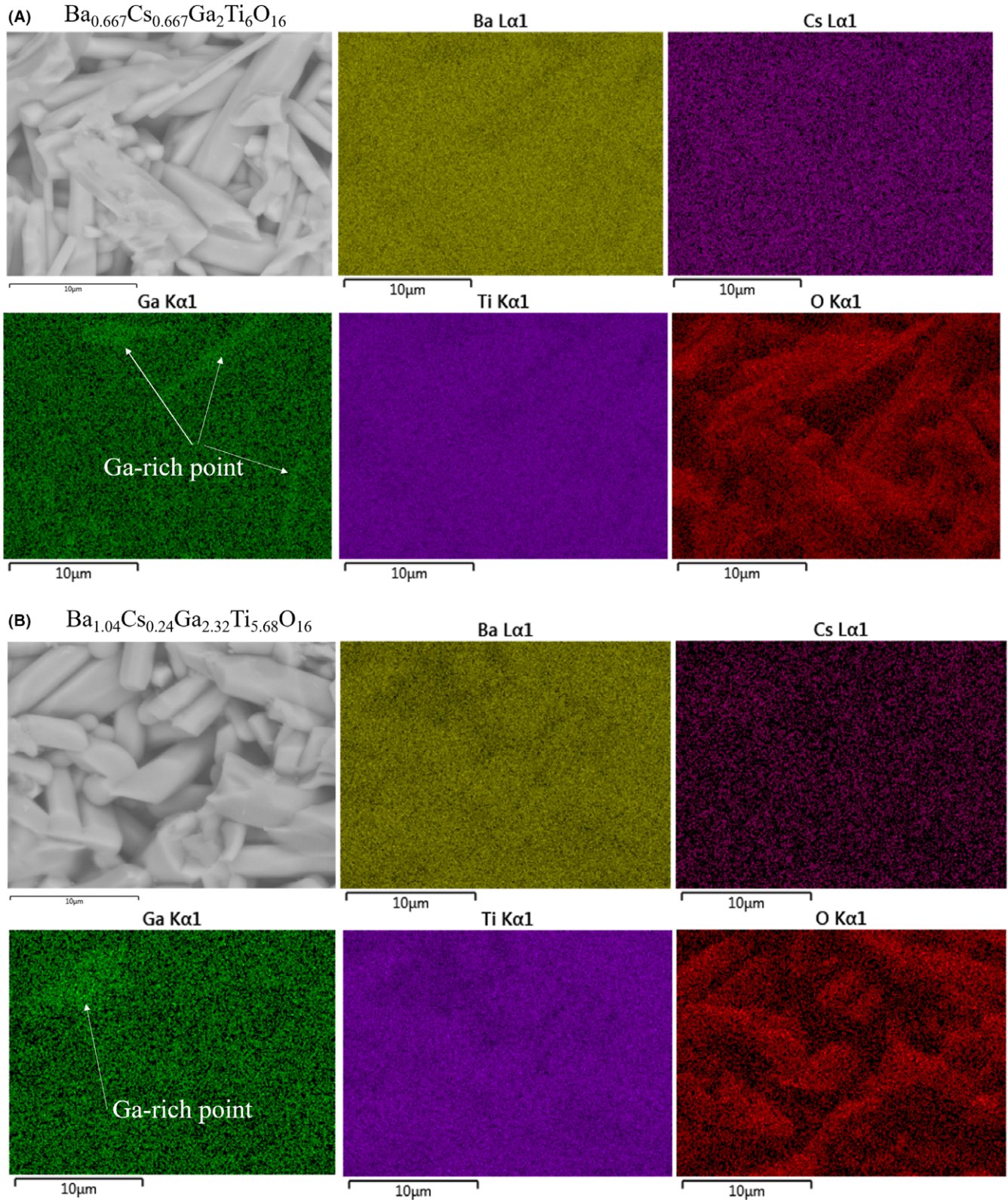


FIGURE 7 The SEM-EDS mapping images of (A) $\text{Ba}_{0.667}\text{Cs}_{0.667}\text{Ga}_2\text{Ti}_6\text{O}_{16}$ (higher Cs content) and (B) $\text{Ba}_{1.04}\text{Cs}_{0.24}\text{Ga}_{2.32}\text{Ti}_{5.68}\text{O}_{16}$ (intermediate Cs content)

and Ga varied greatly between samples. The stoichiometry of Ga reached 3.63 and 3.98 in $\text{Ba}_{0.667}\text{Cs}_{0.667}\text{Ga}_2\text{Ti}_6\text{O}_{16}$ and $\text{Ba}_{1.04}\text{Cs}_{0.24}\text{Ga}_{2.32}\text{Ti}_{5.68}\text{O}_{16}$, which are much higher than

the majority phase's Ga content. In addition, according to charge balance considerations, the amount of Cs at A sites in the minority phase must be greater than that in the

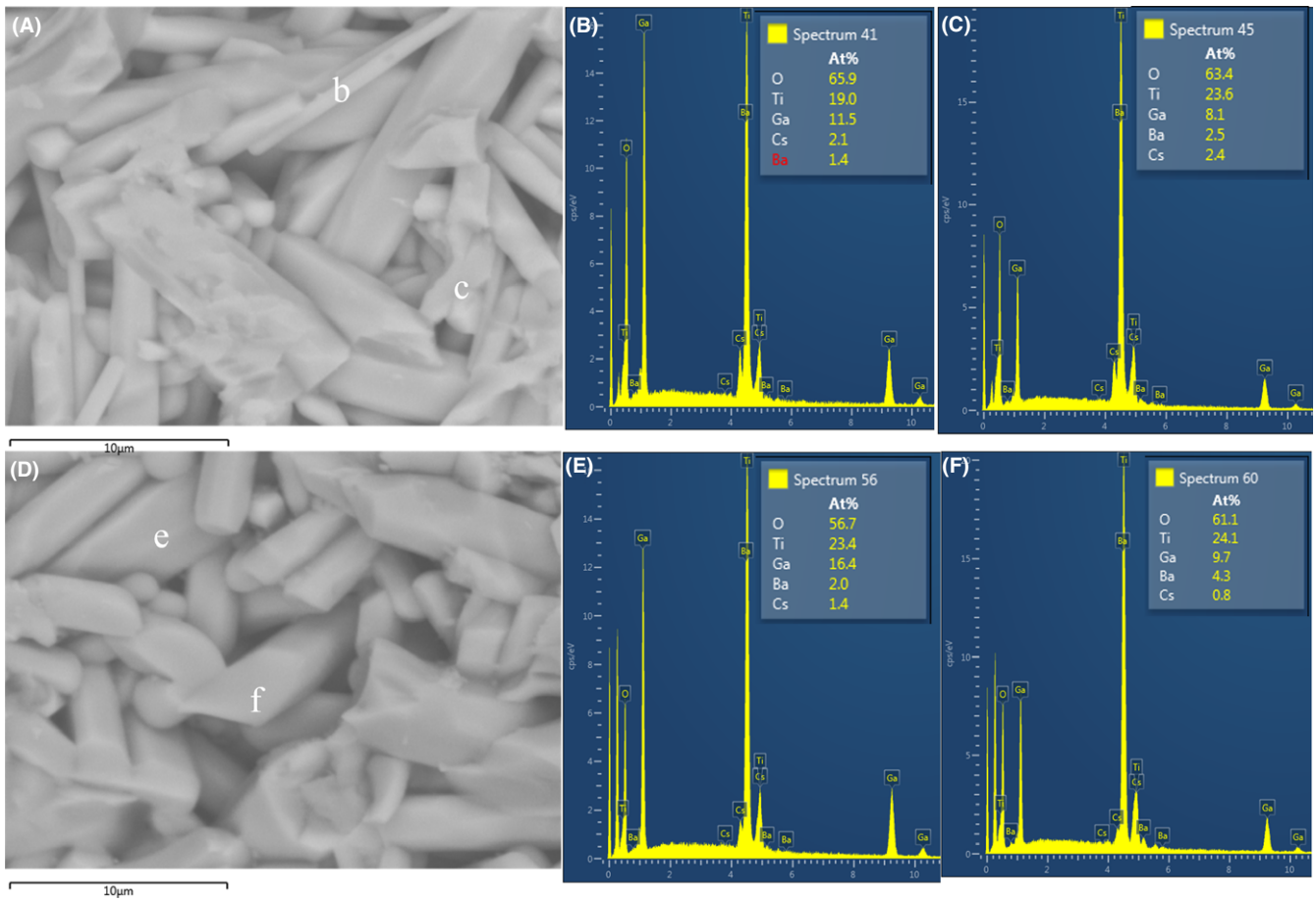


FIGURE 8 The EDS point result of majority and minority phases is list in (A-C) $\text{Ba}_{0.667}\text{Cs}_{0.667}\text{Ga}_2\text{Ti}_6\text{O}_{16}$ and (D-F) $\text{Ba}_{1.04}\text{Cs}_{0.24}\text{Ga}_{2.32}\text{Ti}_{5.68}\text{O}_{16}$

majority. Thus, the Cs concentration at A sites of the minority phase was 20% and 118% higher than the target phase in $\text{Ba}_{0.667}\text{Cs}_{0.667}\text{Ga}_2\text{Ti}_6\text{O}_{16}$ and $\text{Ba}_{1.04}\text{Cs}_{0.24}\text{Ga}_{2.32}\text{Ti}_{5.68}\text{O}_{16}$, respectively. In recent work, it was found that high Cs concentrations represent the most thermodynamically favorable state for these hollandite systems.¹⁷ In light of these findings, one potential explanation of the Ga-rich and Cs-rich phase detected by TXM could be a thermodynamic driving force to form a more stable phase.

The analysis above indicates that the observed rod-like, Ga-rich regions may have different stoichiometries/composition than the primary hollandite phase. The heterogeneous nature of this single-phase hollandite could be expected in a solid-state ceramic processing route where a sample's homogeneity is determined by physical mixing coupled with diffusion and (potentially incomplete) phase reaction processes at elevated temperature. This picture of the materials system would explain why only hollandite was detected by laboratory-based XRD (i.e., because the lattice parameters and the changes between the majority and minority phases of the single hollandite phases were too small to detect), whereas “hot

spots” in local Ga composition were detected by TXM and SEM-EDS.

Using the estimated stoichiometries for the majority and minority hollandite phases, their absorption properties were estimated using the CXRO X-ray calculator and the estimates were compared against the contrast observed in the TXM images. Figure 9 shows the absorption edges calculated for the minority (red), majority (green), and target (blue) hollandite phases. The plots suggest three expectations for the contrast above and below the Ga k-edge: (i) below the edge, the minority phase absorbs less (and transmits more) than the majority phase and, therefore, should appear darker in the below-edge images (TXM images are presented in “reverse contrast”); (ii) above the edge, the minority phase absorbs more and should appear lighter than the majority phase; and (iii) across the edge, the minority phase's change in contrast should be greater than that of the majority phase (a 7% change in the majority phase vs. a 22% change in the minority for the high cesium composition and a 16% vs. a 33% change for the lower cesium composition).

The contrast measured in the TXM images is in fact consistent with the three expectations listed above. For both the

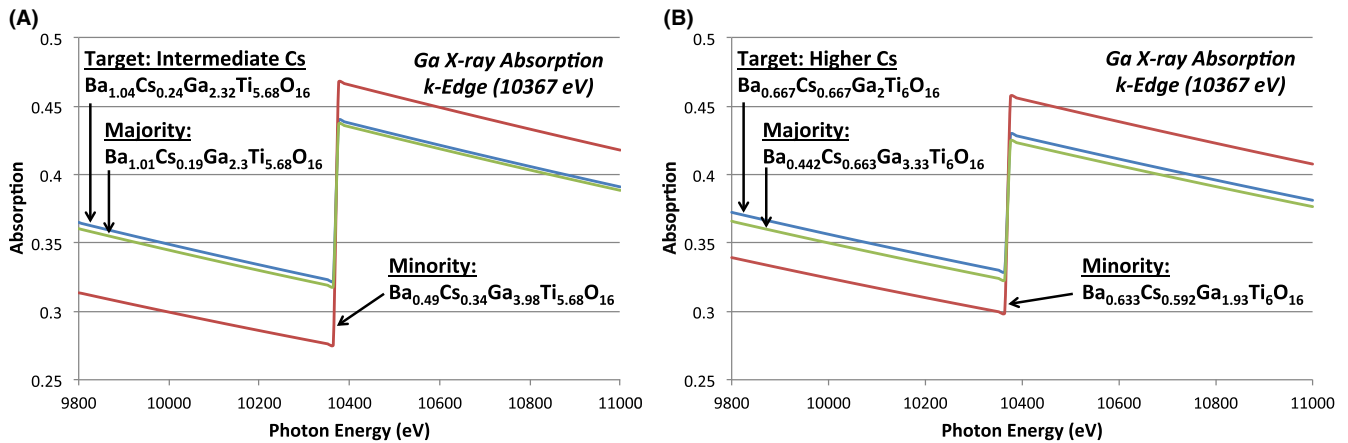


FIGURE 9 Calculated Ga X-ray absorption k-edges for minority, majority, and target hollandite phases in the (A) intermediate and (B) higher Cs-content single-phase hollandite systems

literature Cs and high-Cs samples, the minority hollandite phase appears darker in the below-edge image and lighter in the above-edge. Furthermore, the percent changes in contrast for both samples are consistent with those predicted. The minority phase's contrast changed by 27% and 29% in the literature and high-Cs content samples, respectively. The corresponding predicted changes were 33% and 22%. The contrast changes exhibited by the majority phase in the literature and high-Cs content samples were 13% and 12%, respectively, where the corresponding predicted values were 16% and 7%. Exact agreement between the predicted and measured values was not expected because the CXRO calculator does not take into account porosity. Therefore, the TXM results are consistent with the SEM-EDS analysis that suggested the presence of a majority and minority composition of the same single-phase hollandite.

7 | CONCLUSIONS

In this work, synchrotron-based transmission X-ray microscopy was used to image the 3-D microstructure of multiple phases within model waste form material systems. It was found that Ga-doping levels consistent with those commonly used for nuclear waste immobilization ($\text{Ba}_{1.04}\text{Cs}_{0.24}\text{Ga}_{2.32}\text{Ti}_{5.68}\text{O}_{16}$) could be readily imaged. These results represent an important first step in developing the methods and tools needed to gain an improved understanding of the link between 3-D morphological and chemical features of waste form material microstructures and the corrosion behavior of the materials.

SEM-EDS confirmed the chemical composition of a majority phase and a minority phase in the Ga-doped hollandite waste form material. Three-dimensional absorption contrast TXM images of the samples exhibited contrast changes across the Ga k-edge consistent with the SEM-EDS findings. The analysis suggests that the minority phase is a different

stoichiometry/composition of the primary hollandite phase formed by the solid-state ceramic processing route. In future work, the heterogeneous nature of hollandite formation will be examined as a function of processing techniques including melt and crystallization as well as complementary analytical techniques, for example (but not limited to), X-ray Absorption Near Edge Structure spectroscopy to better understand the chemical nature of these phases.

ACKNOWLEDGMENTS

The authors are grateful for the support of Nuclear Energy University Program of the US Department of Energy Award ID: DE-NE0008260, CFA-14-6357: "A New Paradigm for Understanding Multiphase Ceramic Waste Form Performance." Portions of this research were carried out at the Stanford Synchrotron Radiation Light-source, a national user facility operated by Stanford University on behalf of the U.S. Department of Energy, Office of Basic Energy Sciences. Dr. Ye Lin at the University of South Carolina is gratefully acknowledged for assistance with XPS measurements.

REFERENCES

1. Waste forms technology and performance, Final Report by National Research Council of the National Academies ISBN-10: 0-309-18733-8; 2011.
2. Ringwood A, Kesson S, Ware N, Hibberson W, Major A. Immobilization of high-level nuclear-reactor wastes in SYNROC. *Nature*. 1979;278:219-223.
3. Ringwood AE, Kesson SE, Ware NG, Hibberson WO, Major A. Synroc process—geochemical approach to nuclear waste immobilization. *Geochem J*. 1979;13:141-165.
4. C Natl Res, *Waste Forms Technology and Performance: Final Report*. Washington: Natl Academies Press; 2011.
5. Kerr RA. Nuclear waste-disposal - alternatives to solidification in glass proposed. *Science (80-.)*. 1979;204:289-291.

6. Brinkman K, Fox K, Marra J, Tang M. Crystalline ceramic waste forms: reference formulation report, Savannah River Natl. Lab. Tech. Rep. SRNL-STI-2012-00281, FCRD-SWF-2012-000116; 2012.
7. Carter ML, Gillen AL, Olufson K, Vance ER. HIPed Tailored Hollandite Waste Forms for the Immobilization of Radioactive Cs and Sr. *J Am Ceram Soc.* 2009;92:1112-1117.
8. Cleave A, Grimes RW, Sickafus K. Plutonium and uranium accommodation in pyrochlore oxides. *Philos Mag.* 2005;85:967-980.
9. Brinkman K, Amoroso J, Marra J, Tang M. Crystalline ceramic waste forms: comparison of reference process for ceramic waste form fabrication. SRNL Tech. Report- FCRD-SWF-2013-000229; 2013.
10. Vance ER, Lumpkin GR, Carter ML, et al. Incorporation of uranium in zirconolite ($\text{CaZrTi}_2\text{O}_7$). *J Am Ceram Soc.* 2002;85:1853-1859.
11. Stefanovsky SV, Ptashkin AG, Knyazev OA, Dmitriev SA, Yuditsev SV, Nikonov BS. Inductive cold crucible melting of actinide-bearing murataite-based ceramics. *J Alloys Compd.* 2007;444:438-442.
12. Demine AV, Krylova NV, Polyektov PP, et al., High level liquid waste solidification using a 'cold' crucible induction melter. In: Hart KP, Lumpkin GR, eds. *Scientific Basis for Nuclear Waste Management XXIV*. Warrendale, MI, USA: Materials Research Society; 2000: 27-33.
13. Advocat T, Leturcq G, Lacombe J, et al. Alteration of cold crucible melter titanate-based ceramics: comparison with hot-pressed titanate-based ceramic. In: Gray WJ, Triay IR, eds. *Scientific Basis for Nuclear Waste Management XX*. Warrendale, MI, USA: Materials Research Society, 1997:355-362.
14. Cocco AP, Nelson GJ, Harris WM, et al. Three-dimensional microstructural imaging methods for energy materials. *Phys Chem Chem Phys.* 2013;15:16377-16407.
15. Carter ML, Vance ER, Mitchell DRG, Hanna JV, Zhang Z, Loi E. Fabrication, characterization, and leach testing of hollandite, $(\text{Ba}, \text{Cs})(\text{Al}, \text{Ti})_2\text{Ti}_6\text{O}_{16}$. *J Mater Res.* 2002;17:2578-2589.
16. Amoroso J, Marra J, Conradson SD, Tang M, Brinkman K. Melt processed single phase hollandite waste forms for nuclear waste immobilization: $\text{Ba}(1.0)\text{Cs}(0.3)\text{A}(2.3)\text{Ti}(5.7)\text{O}(16)$; A = Cr, Fe, Al. *J Alloys Compd.* 2014;584:590-599.
17. Xu Y, Wen Y, Grote R, Amoroso J, Nickles LS, Brinkman KS. A-site compositional effects in Ga-doped hollandite materials of the form $\text{Ba}_x\text{Cs}_y\text{Ga}_{2x+y}\text{Ti}_{8-2x-y}\text{O}_{16}$: implications for Cs immobilization in crystalline ceramic waste forms. *Sci Rep.* 2016;6:27412.
18. Kak AC, Slaney M, *Principles of Computerized Tomographic Imaging*. Philadelphia, PA: Society of Industrial and Applied Mathematics; 2001.
19. Markoe A. *Analytic Tomography*. New York, NY: Cambridge University Press; 2006.
20. Liu Y, Meirer F, Williams PA, Wang J, Andrews JC, Pianetta P. TXM-Wizard: a program for advanced data collection and evaluation in full-field transmission X-ray microscopy. *J Synchrotron Radiat.* 2012;19:281-287.
21. Xu Y, Feygenson M, Page K, Shuller-Nickles L, Brinkman K. Structural evolution in hollandite solid solutions across the A-site compositional range from $\text{Ba}_{1.33}\text{Ga}_{2.66}\text{Ti}_{5.34}\text{O}_{16}$ to $\text{Cs}_{1.33}\text{Ga}_{1.33}\text{Ti}_{6.67}\text{O}_{16}$. *J Am Ceram Soc.* 2016;99:4100-4106.
22. Suzuki-Muresan T, Vandenborre J, Abdelouas A, Grambow B, Utsunomiya S. Studies of (Cs, Ba)-hollandite dissolution under gamma irradiation at 95°C and at pH 2.5, 4.4 and 8.6. *J Nucl Mater.* 2011;419:281-290.
23. Kesson SE, White TJ. Radius ratio tolerance factors and the stability of hollandite. *J Solid State Chem.* 1986;63:122-125.
24. Lan C, Gong J, Liu S, S Y. Synthesis and magnetic properties of single-crystalline $\text{Na}(2-x)\text{Mn}(8)\text{O}(16)$ nanorods. *Nanoscale Res Lett.* 2011; 6:1-6.
25. Gionco C, Livraghi S, Maurelli S, et al. Al- and Ga-doped TiO_2 , ZrO_2 , and HfO_2 : the nature of O 2p trapped holes from a combined electron paramagnetic resonance (EPR) and density functional theory (DFT) study. *Chem Mater.* 2015;27:3936-3945.

SUPPORTING INFORMATION

Additional Supporting Information may be found online in the supporting information tab for this article.

How to cite this article: Cocco AP, DeGostin MB, Wrubel JA, Damian PJ, et al. Three-dimensional mapping of crystalline ceramic waste form materials. *J Am Ceram Soc.* 2017; 00:1–14. <https://doi.org/10.1111/jace.14885>